Application of gradient severe shot peening as a novel mechanical surface treatment on fatigue behavior of additively manufactured AlSi10Mg

Erfan Maleki [a], Sara Bagherifard [a,*], Asghar Heydari Astaraee [a], Simone Sgarbazzini [a], Michele Bandini [b], Mario Guagliano [a]

[a] *Department of Mechanical Engineering, Politecnico di Milano, Milano, Italy*
[b] *Peen Service Srl, Bologna, Italy*

ARTICLE INFO

ABSTRACT

Post-processing methods can be crucial in addressing the associated anomalies of the as-built state of additively manufactured materials. In this study, for the first time, the effects of gradient severe shot peening as a novel mechanical surface treatment, along with other types of shot peening treatments, including conventional, severe, and over shot peening processes were investigated individually and combined with heat treatment on fatigue behavior of hourglass AlSi10Mg samples fabricated by laser powder bed fusion. Detailed experimental characterizations in terms of microstructure, porosity, surface texture, hardness and residual stresses as well as rotating bending fatigue behavior were conducted. The experimental results revealed a significant fatigue behavior improvement after applying gradient severe shot peening treatments due to their remarkable capacity to modulate surface texture, known as a side effect of peening, besides surface layer nanocrystallization, enhanced hardness, and high compressive residual stresses.

1. Introduction

As-built (AB) configurations of metallic materials fabricated by additive manufacturing (AM) exhibit microstructural anisotropy [1,2] and volumetric defects [3], as well as high surface imperfections [4]. These defects potentially affect the performance of the AM materials in terms of wear and corrosion resistance as well as their fatigue behavior negatively. Notably, under cyclic loading, surface defects act as local stress concentration zones resulting in early crack initiation and thus early fatigue failure [5]. Hence, post-processing methods are essential to address these challenges [6].

Several impact-based surface treatments have been proposed as nonsubtractive post-treatments for addressing surface flaws in AM. These treatments include shot peening (SP) [7,8], ultrasonic shot peening (USP) [9], cavitation peening (CP) [10,11], ultrasonic shot peening (USP) [12], laser shock peening (LSP) [13–16], and ultrasonic nanocrystal surface modification (UNSM) [17,18].

In our previous studies, we extensively examined the impact of various post-treatments on the microstructure, porosity, surface characteristics, mechanical properties, and fatigue performance of AlSi10Mg produced through AM. These post-treatments included ultrasonic
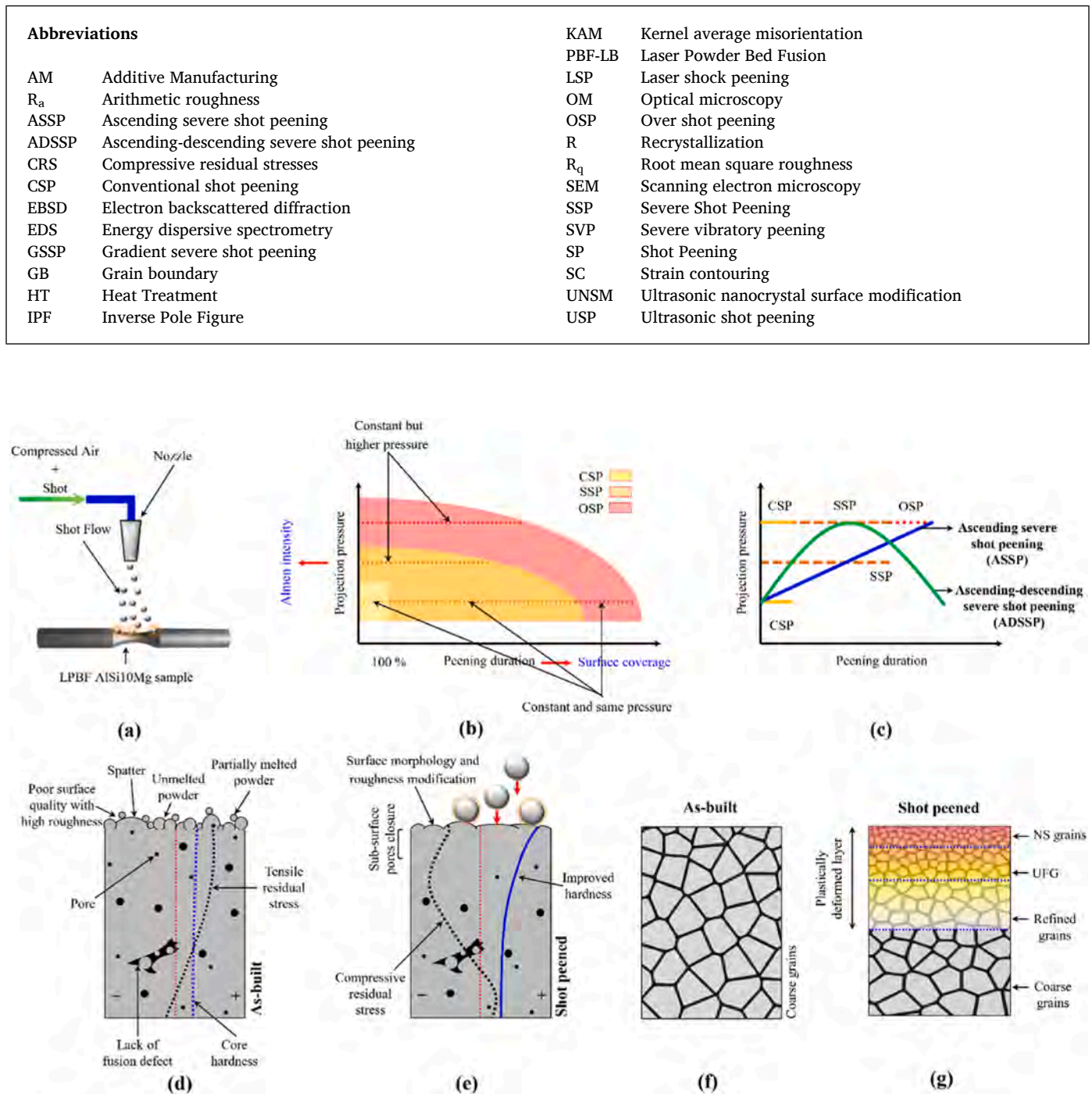
nanocrystal surface modification (UNSM) [19], USP [19], severe shot peening (SSP) [19], severe vibratory peening (SVP) [19,20], laser shock peening (LSP) [21–23], chemical polishing (CP) [24], electro-chemical polishing (ECP) [24], as well as hybrid treatments such as LSP + UNSM [21], SP + ECP [25], UNSM + ECP [25], and SVP + ECP [25]. The objective was to comprehensively investigate their effects on mechanical performance of AM materials. Dealing with the effects of different impact-based surface treatments, the findings revealed that these post-processing methods had a significant influence on both the internal structure and surface characteristics of the treated material. Among the treatments, UNSM exhibited the highest efficacy in enhancing fatigue behavior (i.e., 55-fold increase in fatigue life compared to the as-built state when subjected to a fixed stress level of 110 MPa), followed by SVP, USP, and SSP treatments that resulted in fatigue life improvements of 43, 33, and 28 times higher than the as-built state, respectively [19].

Among different post-treatments, peening-based approaches such as SP have been widely used on AM materials due to their low cost, simplicity, and efficiency in improving mechanical properties [7,26,27]. In the SP process, the material's surface is bombarded by small impacting media under controlled conditions.

Fig. 1a reveals the schematic illustration of the SP process applied on

Abbreviations

|			
		KAM	Kernel average misorientation
		PBF-LB	Laser Powder Bed Fusion
AM	Additive Manufacturing	LSP	Laser shock peening
R_a	Arithmetic roughness	OM	Optical microscopy
ASSP	Ascending severe shot peening	OSP	Over shot peening
ADSSP	Ascending-descending severe shot peening	R	Recrystallization
CRS	Compressive residual stresses	R_q	Root mean square roughness
CSP	Conventional shot peening	SEM	Scanning electron microscopy
EBSD	Electron backscattered diffraction	SSP	Severe Shot Peening
EDS	Energy dispersive spectrometry	SVP	Severe vibratory peening
GSSP	Gradient severe shot peening	SP	Shot Peening
GB	Grain boundary	SC	Strain contouring
HT	Heat Treatment	UNSM	Ultrasonic nanocrystal surface modification
IPF	Inverse Pole Figure	USP	Ultrasonic shot peening

Fig. 1. (a) Schematic illustration of the SP process applied to an AM part (b) comparison of different CSP, SSP and OSP processes concerning the values of Almen intensity and surface coverage. (c) Comparison of the CSP, SSP, OSP, ASSP and ADSSP processes considering projection pressure and peening duration. Schematic illustration comparing the surface morphology, porosity, hardness and residual stresses of AM materials in (f) as-built condition and (g) after applying SP-based treatments. Schematic illustration of comparison of the microstructure of AM materials in (f) as-built state and (g) after applying SP-based treatments.

an AM part. SP induces grain refinement, hardening and compressive residual stresses (CRS) in the surface layer [28]. However, due to the shot impacts and formation of dimples and craters with overlaps, the surface morphology of the material can be considerably altered after SP [29].

Generally, the SP process can be controlled via Almen intensity and surface coverage parameters, which can be assessed by air projection pressure and peening duration, respectively. Severe shot peening (SSP) can be achieved by enhancing the kinetic energy of the SP process via increasing Almen intensity and surface coverage in comparison with the

parameters used the conventional shot peening (CSP) [30,31].

SSP has been reported to have more beneficial effects than CSP in terms of mechanical properties and fatigue behavior improvement due to surface layer nanocrystallization and inducing higher and deeper CRS [32–38]. On the other hand, by employing higher levels of Almen intensity and coverage than the optimized and favorable ones used in SSP, over shot peening (OSP) can be obtained. OSP was found to detrimentally affect fatigue strength due to excessively high surface roughness and the formation of various surface defects such as nano/micro-cracks [39–43]. Fig. 1b compares the ranges of Almen intensity and surface
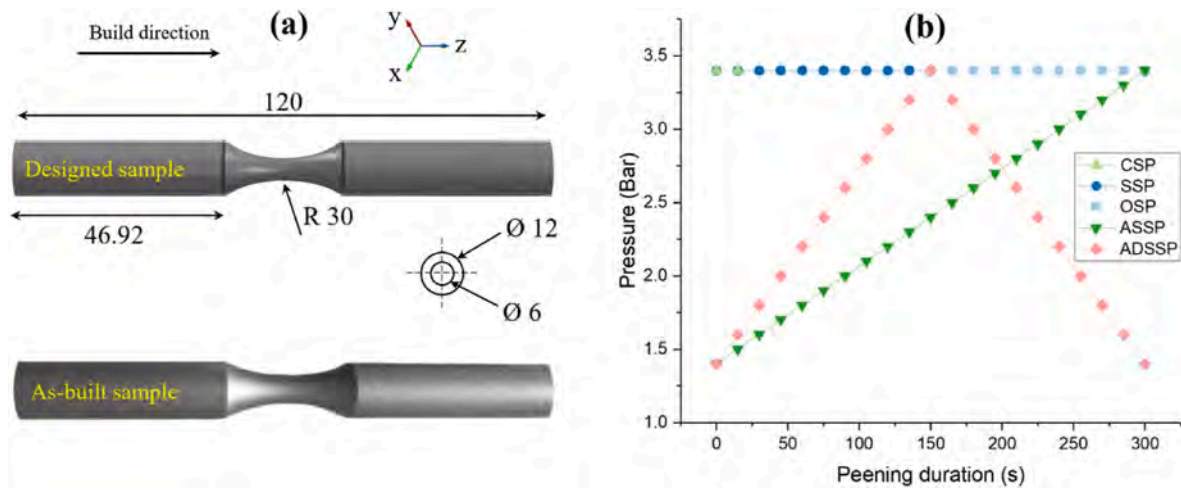
Fig. 2. (a) Shape and size of the as-designed and as-built hourglass PBF-LB AlSi10Mg samples. (b) The corresponding projection pressure and peening duration of different applied SP treatments of CSP, SSP, OSP, ASSP and ADSSP.

coverage used for CSP, SSP and OSP processes.

We recently introduced a novel SP-based treatment named gradient severe shot peening (GSSP), designed to avoid the negative influences of OSP, while taking advantage of surface layer nano-crystallization, hardening and high CRS. When applied to classic bulk materials, the suggested GSSP treatment improved fatigue strength considerably [44].

In the GSSP process, variant pressures are used instead of employing constant projection pressures during the peening process. According to the trends of considered pressure variation, two different GSSP processes of ascending severe shot peening (ASSP) and ascending-descending severe shot peening (ADSSP) were suggested [44]. Fig. 1c schematically compares the CSP, SSP, OSP, ASSP and ADSSP processes considering projection pressure and peening duration. Fig. 1d and e depict the effects of SP treatment on as-built AM material in terms of surface morphology modification, sub-surface pore closure, hardening, and induced CRS. In addition, surface grain refinement after SP treatment compared to the as-built AM material is indicated in Fig. 1f and g.

In this particular investigation, the authors aimed to explore the effects of a novel post-processing technique of GSSP on an AM material. It is worth noting that, to the best of the authors' knowledge, this study represents the first investigation of GSSP in AM field. Herein, comprehensive experimental approaches were implemented to thoroughly analyze and understand the impact of various SP treatments on hourglass-shaped laser powder bed fused (PBF-LB) AlSi10Mg samples. The SP treatments investigated are CSP, SSP, OSP, ASSP and ADSSP. The experiments were designed to assess multiple factors, including the microstructure, porosity, surface roughness and morphology, hardness, residual stresses, and fatigue behavior of the samples. The acquired results were subjected to critical analysis and thorough discussion, emphasizing the advantages and benefits offered by the GSSP approach. The unique strengths and benefits of the GSSP method are discussed in detail.

By shedding light on the effects of GSSP on AM materials and comparing its performance with other SP treatments, this study contributes to the existing body of knowledge in the field. It is important to highlight that this study builds upon our previous studies, which focused on investigating the impacts of various post-processing techniques on the surface characteristics, mechanical properties, and fatigue strength of PBF-LB AlSi10Mg. Relying upon our previous work, we aim to gain further insights into the potential of post-processing techniques for improving the overall performance of PBF-LB AlSi10Mg specimens/components.

Table 1
The parameters of the SP treatments for CSP, SSP, OSP, ASSP and ADSSP.

SP treatment	Shot diameter (mm)	Projection pressure (Bar)	Almen intensity (0.01 inch A)	Peening duration (s)	Surface Coverage (%)
CSP	0.43	3.4	14	15	100
SSP	0.43	3.4	14	150	1000
OSP	0.43	3.4	14	300	2000
ASSP	0.43	$1.4 \rightarrow 3.4$	$7 \rightarrow 14$	300	–
ADSSP	0.43	$1.4 \rightarrow 3.4 \rightarrow 1.4$	$7 \rightarrow 14 \rightarrow 7$	300	–

2. Material and methods

Cylindrical hourglass fatigue test specimens were manufactured using PBF-LB with gas-atomized spherical powder of AlSi10Mg having a mean particle diameter of 50 μm. The specimens were fabricated in the vertical direction using SLM 500 HL system equipped with Yttrium fiber lasers applying optimized processing parameters stated in Ref. [45]. The shape and size of the as-designed and as-built specimens are depicted in Fig. 2a.

The specimens were treated using various SP treatments, including CSP, SSP, OSP, ASSP, and ADSSP, as well as their combination with heat treatment (HT). Microstructural homogenization and relaxation of tensile residual stresses in the as-built condition were achieved using T6 HT based on the time and temperature cycles reported in our previous study [46]. The SP treatments were performed in an air blast SP machine using standard S170 steel shots and with a 10 cm of stand-off distance. The related projection pressures and peening durations are shown in Fig. 2b. Almen intensity was measured using Almen strips of type A following the procedure in the SAE J443 standard [47].

The SP process parameters are listed in detail in Table 1. The peening interval for both ASSP and ADSSP was set to be identical to the one of OSP, which was the longest exposure time (300 s). It is worth mentioning that it was not straightforward to measure the peening coverage for GSSP treatments based on the standard methodologies mainly due to the gradual variation in pressure during the treatment, which directly influenced the dimensions of the formed dimples on the surface. Thus, a time interval equal to 15 s, corresponding to 100% peening coverage with constant pressure on the same specimens, was selected as the basis for the variation of the projection pressure for GSSP treatments.

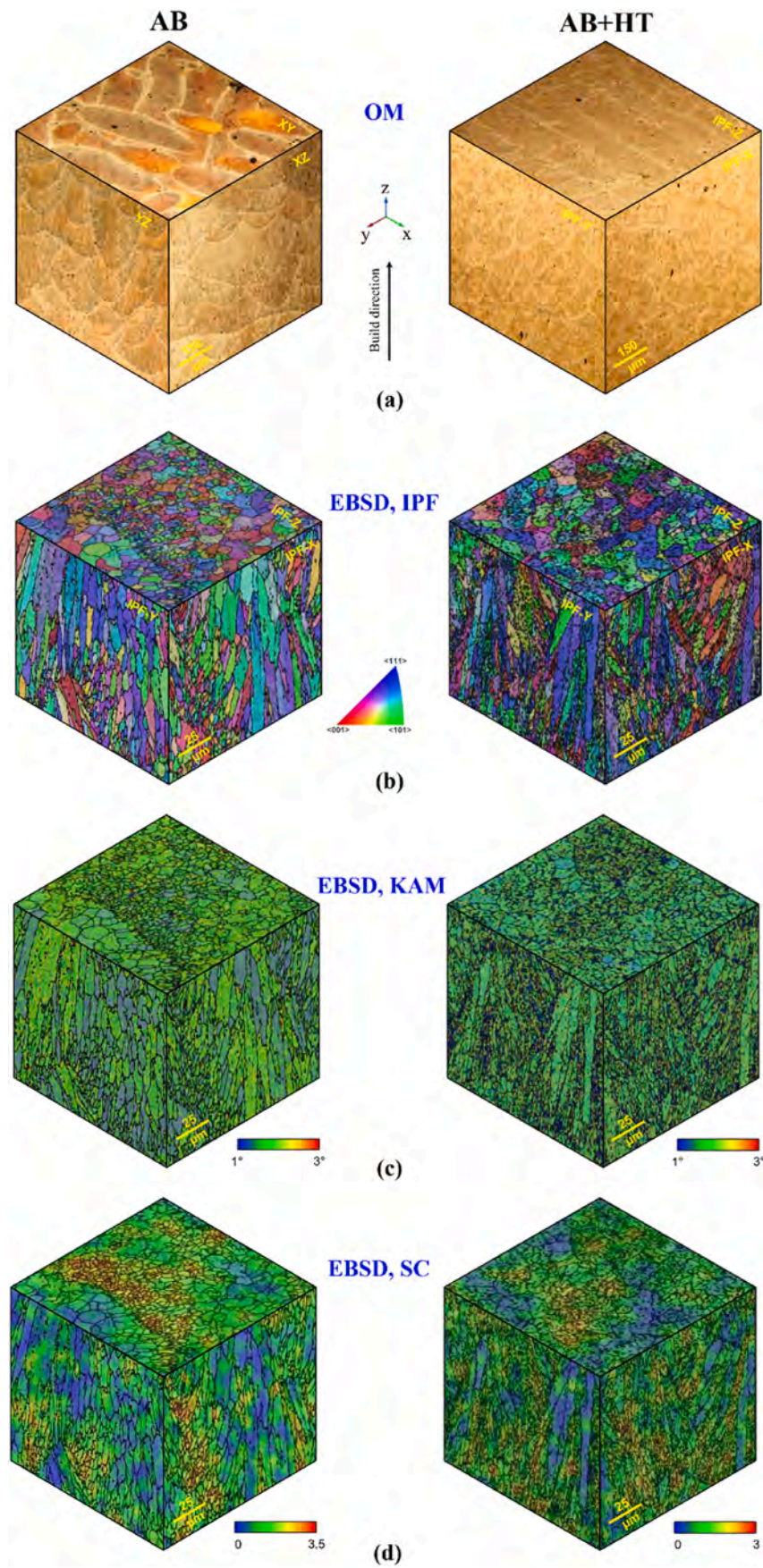12 sets of samples including AB, AB + CSP, AB + SSP, AB + OSP, AB

Fig. 3. Typical microstructure of as-built (left row) and heat treated (right row) samples obtained by (a) OM, and (b) IPF, (c) KAM, and (d) SC maps achieved by EBSD.
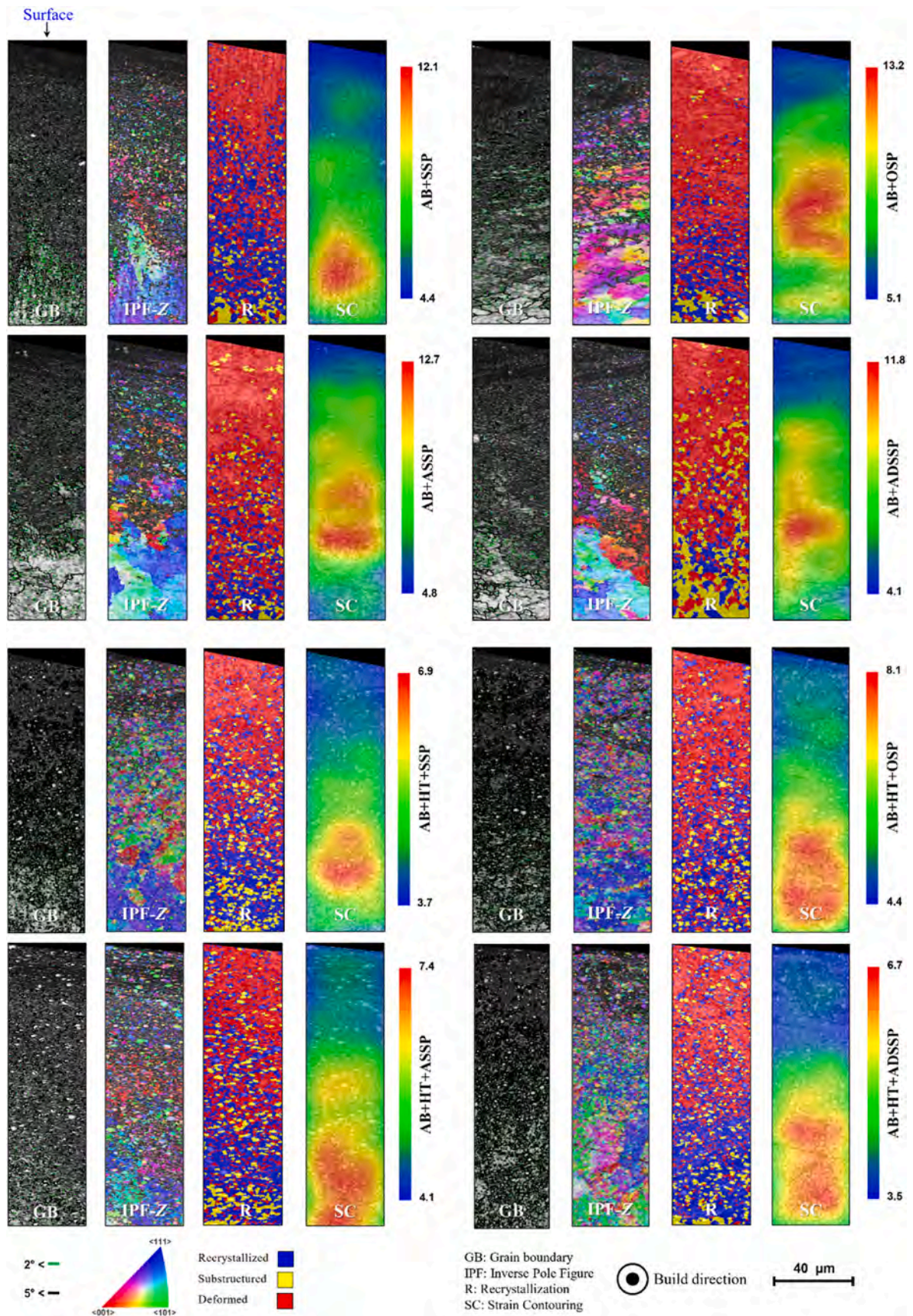
Fig. 4. EBSD results regarding GB, IPF, R and SC in the surface layer of the samples subjected to different peening treatments.

+ ASSP, AB + ADSSP, AB + HT, AB + HT + CSP, AB + HT + SSP, AB + HT + OSP, AB + HT + ASSP, and AB + HT + ADSSP were studied to evaluate the sole and hybrid effects of the applied post-treatments.

Microstructural investigations were carried out using Nikon Eclipse LV150NL optical microscope and high-resolution Zeiss Sigma 500 VP field-emission scanning electron microscope equipped with electron backscattered diffraction (EBSD) and energy dispersive spectrometry (EDS). The section of the samples was cut longitudinally and transversally with respect to the build direction and the polished cross-sections were etched chemically for 20 s with Keller's reagent. The Al matrix was solely taken into account to obtain high-resolution EBSD results. Inverse pole figure (IPF-Z), Kernel average misorientation (KAM), and strain contouring (SC) maps were captured by processing EBSD data in AZtecHKL software following the approach for EBSD sample characterization in our previous study [48].

Porosity was measured based on image analysis using optical microscopy (OM) images. The method developed by Kim et al. [49] was employed for binarizing the images for local thresholding and attaining the highest clarity of the smaller pores.

Surface morphology was studied by a Zeiss EVO50 scanning electron microscope and Alicona Infinite Focus confocal microscope with a lateral resolution of 0.10 μm and a vertical resolution of 10 nm. Surface roughness quantification was performed based on the ISO 25178-2 standard [50] in terms of the arithmetic mean (R_a) and root mean square (R_q) parameters.

Microhardness was measured on the polished transversal cross-sections (*xy*-plane) using a Leica WMHT30A micro-Vickers indentation testing machine with a load of 25 gf, dwell time of 15 s and a 50 μm distance between indentations. The microhardness values were averaged based on three different measurements at each depth.

Residual stress profiles were acquired using AST X-Stress 3000 portable X-ray diffractometer equipped with CrKα radiation. In-depth profiles were obtained on a path perpendicular to the build direction from the surface through the core up to a depth of 750 μm. Thin layers of material were removed by electrochemical polishing in a solution of acetic acid (94%) and perchloric acid (6%) and at a voltage of 40 V before each in-depth X-ray diffraction.

All sets of samples were exposed to rotating bending fatigue tests using the Italsigma testing machine with a constant amplitude stress of 110 MPa, a run-out limit of 1×10^7 cycles, a stress ratio of R = −1 and a rotational speed of about 2500 rpm. The fatigue test was repeated three times for each set and thus the average fatigue lives were reported. The fractography analysis of the fracture surfaces was performed using Zeiss EVO50 scanning electron microscopy (SEM).

3. Results and discussions

This section of the study presents the findings obtained from various analyses conducted to evaluate material properties before and after applied HT and SP processes. These analyses include microstructural examination, porosity assessment, surface morphology and roughness characterization, microhardness measurement, residual stress evaluation, and fatigue behavior analysis.

Microstructural analyses were performed to gain insights into the internal structure of the material in terms of isotropy and influence of post-treatments. This involved investigating the arrangement and distribution of the constituent phases, grain size, and any potential defects or anomalies present within the microstructure. Porosity analyses were conducted to quantify the extent of internal defects within the material. The aim was to assess the quality and integrity of the fabricated samples and determine the extent of porosity, as excessive porosity can significantly impact the mechanical performance of the material. Surface morphology and roughness analyses were carried out to examine the external appearance and texture of the material's surface. Parameters such as surface roughness and topographical features were measured and analyzed to understand the quality of the surfaces before and after

applying SP treatments. Microhardness measurements were performed to determine the material's hardness variation in depth at a microscopic scale. This measurement provides valuable information about the material's resistance to deformation and its overall strength characteristics. Residual stress measurements were conducted to assess the presence of any internal or introduced stresses due to the fabrication process and surface treatments. These residual stresses can influence the material's mechanical properties and potentially affect its performance under different loading conditions. Finally, the fatigue behavior of the material was investigated. The results obtained from these comprehensive analyses provide valuable insights into the material's properties and performance characteristics affected by the designed post-processing methods.

3.1. Microstructural analyses

As in this study, half of the samples were heat treated; firstly, the AB and AB + HT samples were characterized by their microstructure using OM and EBSD methods. Fig. 3a reveals the OM images of the typical microstructure of the AB and AB + HT samples demonstrating the removal of melt pool boundaries after applying HT. Fig. 3b indicates the IPF maps and crystallographic orientation of the AB and AB + HT samples showing epitaxial columnar grain growth parallel to the build direction as the solidification of PBF-LB materials occurs along the build direction due to the favorable direction of heat transfer [51–53]. In addition, the formation of small equiaxed grains around the melt pool boundaries can be observed, which is a common phenomenon in PBF-LB materials [54]. Fig. 3c shows the KAM maps of AB and AB + HT samples. The results indicate the occurrence of stress relief after applying HT based on the mean KAM values of 0.67 and 0.51° for AB and AB + HT samples, respectively. SC maps indexing strain variations was also achieved for AB and AB + HT samples, as presented in Fig. 3d. The results indicate higher strains around the melt pool boundaries where the density of equiaxed grains is relatively higher. Lower maximum localized strain values of 3 were obtained for the AB + HT samples compared to the AB ones with a maximum strain of 3.5 due to considerable strain release after HT.

The microstructure in the surface layers of the samples subjected to different SP treatments was also characterized by EBSD considering a scan area of 40×120 μm^2 on transversal (*xy* plane) cross-section, as illustrated in Fig. 4. Grain boundary (GB) maps reveal a very high density of grain boundaries on the top surface layer as a result of grain refinement to different extents after applying SP treatments. IPF-*Z* maps indicate the formation of gradient microstructures with a gradual increase in grain size from nano-crystallized grains in the top surface to the coarse grains through the bulk material in the samples. As a scanning step size of 0.1 μm was considered for EBSD characterization, the nanostructured grains (with grain size <100 nm) were not detected and zero solutions were shown in black. In addition, it can be observed that in the shot peened samples with as-built initial states, the depths of nanostructured layers are higher than the ones with initial heat treated conditions (due to higher ductility of heat treated states). The results reveal that OSP had the most increased effects on surface layer nano-crystallization (in terms of depth from the surface), followed by ASSP, SSP and ADSSP, respectively, for both as-built and heat treated initial states.

Dynamic recrystallization (R) maps show the formation of deformed grains in the top surface layer, which gradually decreased through the interior and were replaced with recrystallized and substrutured grains. The SC maps indicated significant plastic strains due to surface severe plastic deformation in the SP treated samples. The maximum localized plastic strains of 12.1, 13.2, 12.7, 11.8, 6.9, 7.4, 8.1, and 6.7 were obtained for AB + SSP, AB + OSP, AB + ASSP, AB + ADSSP, AB + HT + SSP, AB + HT + OSP, AB + HT + ASSP, and AB + HT + ADSSP samples, respectively. It should be noted that the occurrence of maximum values of induced plastic strains in the sub-surface is expected in the materials
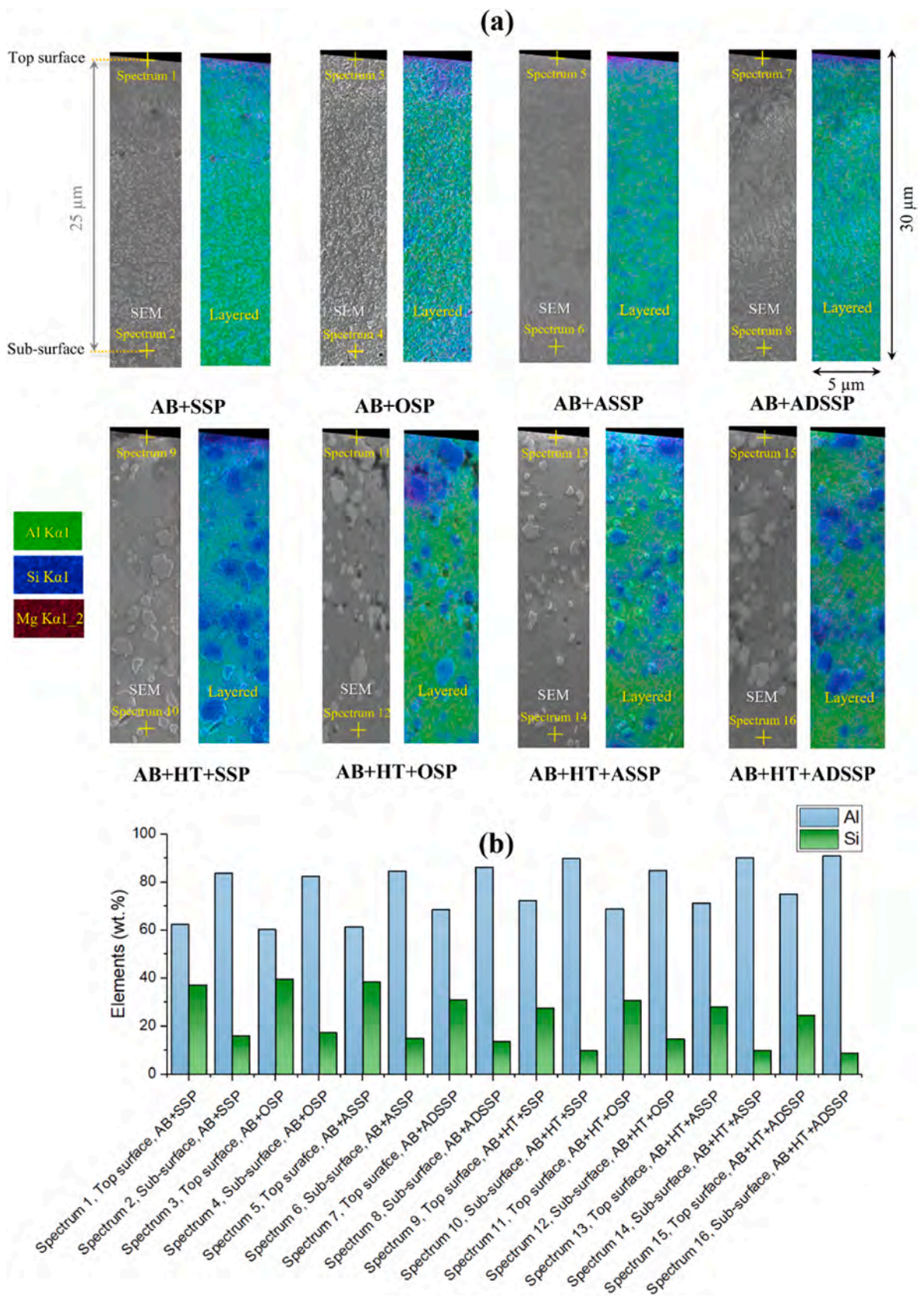
Fig. 5. (a) Layered EDS maps of shot peened samples. (b) Chemical composition by EDS point analysis in the top and sub-surface layer of the shot peened samples.
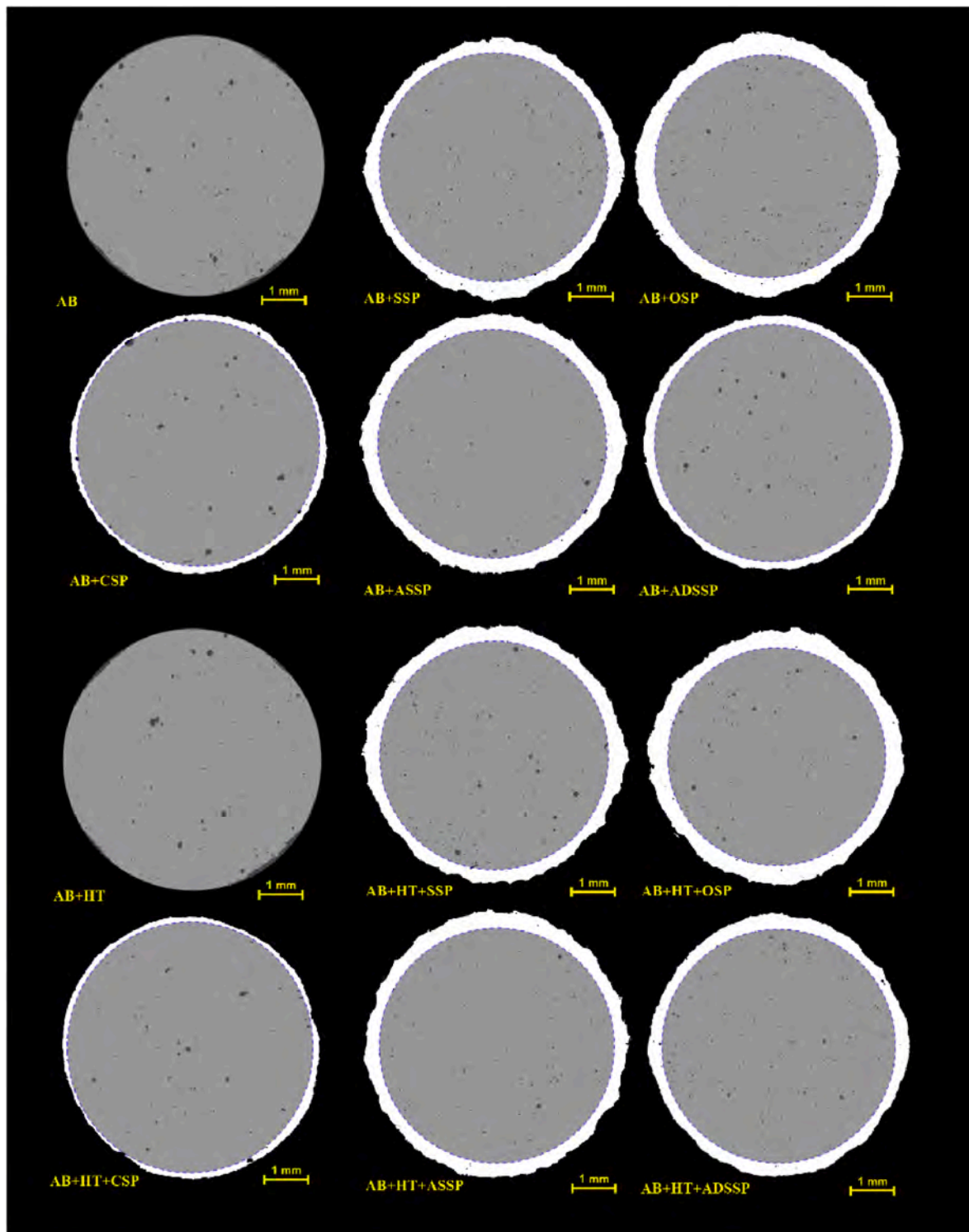
Fig. 6. OM image-based porosity analyses of all sets of samples considering sub-surface pore closure in the shot peened series.

subjected to plastic deformation methods [55–57].

Our previous studies on PBF-LB materials subjected to surface severe plastic deformation indicated that apart from the formation of microstructural gradient caused by surface layer grain refinement, a chemical gradient of the Si phase in the surface layer can also occur [20]. Hence, in this study, EDS point and map analyses were carried out on the shot peened samples to survey this phenomenon, as presented in Fig. 5a. Two spectrum points were considered in a scan area of 5×30 µm² considering one spectrum point on top of the peened surface layer and another

one in the sub-surface, 25 µm below the surface. As can be seen in the layered EDS maps, the fraction of the Si phase (blue phase) is increased to different extents considerably compared to the deeper parts, while the Al phase (green phase) was reduced after SP treatments.

Moreover, a transformation of fibrous Si networks in the as-built state to spherical Si particles in the heat-treated configuration can be observed. Fig. 5b shows the quantitative results of EDS analyses for fractions of Al and Si phases. In the top surfaces, Si weight percentages of 37.2, 39.6, 38.5, 31.5, 27.4, 30.7, 28.1 and 24.7% and 31.7% were
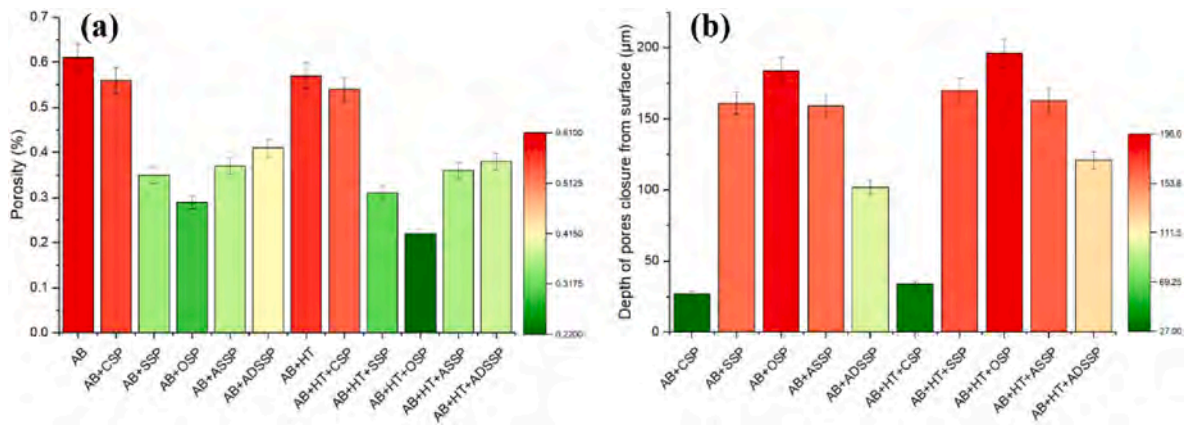
Fig. 7. Quantitative results of porosity measurements in terms of (a) mean porosity and (b) depth of pore closure for all sets of samples.

obtained for AB + SSP, AB + OSP, AB + ASSP, AB + ADSSP, AB + HT + SSP, AB + HT + OSP, AB + HT + ASSP and AB + HT + ADSSP samples, respectively. At the same time, Si weight percentages of 13.5–17.3 and 8.8–14.7% were achieved in the sub-surface of the peened samples with initial as-built and heat-treated states, respectively. Increasing Si content in Al–Si alloys can improve the tensile strength, hardness, and tribological properties but leads to decreased elongation [58–62]. The simultaneous formation of microstructural and chemical gradients revealed by EBSD and EDS results can lead to enhanced performance and local surface layer strengthening.

3.2. Porosity analyses

Fig. 6 illustrates the merged and binarized OM images of transversal cross-sections (xy-plane) that were used for porosity measurement on the mid-section of all samples. In the images, the white area (represented by a white ring) corresponds to the region where pores have been closed because of the induced severe plastic deformation by SP treatments. For porosity analysis, three different samples from each set were selected. The mean porosity values were determined for various sample sets of AB, AB + CSP, AB + SSP, AB + OSP, AB + ASSP, AB + ADSSP, AB + HT, AB + HT + CSP, AB + HT + SSP, AB + HT + OSP, AB + HT + ASSP and AB + HT + ADSSP and the mean porosity values obtained were 0.61, 0.56, 0.35, 0.29, 0.37, 0.41, 0.57, 0.54, 0.31, 0.22, 0.36 and 0.38% respectively, as shown in Fig. 7a. It is worth noting that the application of high-intensity SP treatments has been previously reported to result in a reduction in mean porosity, which aligns with the findings of this study [8]. Additionally, Fig. 7b illustrates the effects of different treatments on sub-surface pore closure in both the as-built and heat-treated states. It is evident from the figure that OSP had the most significant impact on closing sub-surface pores, followed by SSP, ASSP, ADSSP and CSP treatments for both as-built and heat-treated samples.

This phenomenon can be attributed to several mechanisms associated with the impact of high-velocity shot particles on the material's surface: (i) when SP is applied to AM materials, the high-energy impacts of the shot particles create compressive stress waves that propagate beneath the surface. These stress waves induce plastic deformation in the material, causing localized surface expansion. As a result, the material experiences CRS near the surface, which can contribute to sub-surface pore closure; (ii) moreover, during the SP process (or other impact-based techniques such as UNSM, USP, etc.), the plastic deformation and compression of the material promote the movement and rearrangement of its microstructural features, including pores. The high intensity impacts of the shot particles exert pressure on the material, leading to the closure of sub-surface pores. This closure occurs as the material's particles are displaced, pressed, and rearranged, effectively reducing the size and accessibility of the pores; (iii) additionally, the plastic deformation induced by SP can result in a densification effect in the

surface layer (as shown in Figs. 4 and 5). As the shot particles strike the surface of material, they create localized deformation zones that cause the material to flow and compact. This compaction effect contributes to pore closure by squeezing and compacting the material around the pores, reducing their size and diminishing their connectivity. By promoting plastic deformation and compaction in the material, SP, like other mechanical surface treatments, facilitates the closure of sub-surface pores in AM materials. Overall, the combination of compressive stress waves, plastic deformation, and densification effects induced by high-velocity impacts helps minimizing porosity and improving mechanical properties, and fatigue resistance of the material.

3.3. Surface morphology and roughness analyses

Surface morphologies of the AB series and SP treated samples obtained from SEM and confocal microscopy observations are presented in Fig. 8a. Different types of surface imperfections, including randomly positioned unmelted and partially melted powders as well as spatters can be observed on the surface of AB and AB + HT samples. However, these surface defects were considerably removed after applying SP treatments resulting in highly uniform surface morphologies with a particular pattern of dimples and overlaps typical of the SP process. Fig. 8b depicts the surface roughness measurement results regarding R_a and R_q. The results reveal that R_a values of AB and AB + HT samples with 9.34 and 9.26 μm, respectively, were reduced after applying CSP, SSP, ASSP and ADSSP down to 6.1, 8.68, 8.34, 5.23, 7.70, 8.91, 7.59 and 5.68 μm for AB + CSP, AB + SSP, AB + ASSP, AB + ADSSP, AB + HT + CSP, AB + HT + SSP, AB + HT + ASSP and AB + HT + ADSSP samples, respectively. However, the surface roughness values after OSP were enhanced to 10.12 and 12.02 μm for AB + OSP, and AB + HT + OSP samples, respectively, exhibiting adverse effects of OSP on surface roughness modification. In addition, the surface roughness of the samples with initial as-built configuration is lower than the ones with initial heat-treated states. This can be attributed to the lower strength of heat-treated samples allowing the different SP treatments to form deeper dimples on the treated surfaces. It should be noted that other roughness parameters, such as Rq values that are not presented for brevity, showed a similar trend with R_a. Fig. 8c illustrates the effects of each SP treatment on surface roughness variation in terms of R_a compared to the as-built state. It can be noted that ADSSP had the most decisive influence on surface roughness reduction with −44 and −39% roughness variation in AB + ADSSP and AB + HT + ADSSP samples, respectively.

Gradual raising of the projection pressure in the ASSP and ADSSP treatments with the same peening duration of OSP acts as a pre-hardening stage for the subsequent higher pressures, which leads the material to avoid forming high surface roughness and surface defects. During ASSP, on the other hand, as the pressure grows ascendingly during the exposure time, instead of forming dimple-shaped surface
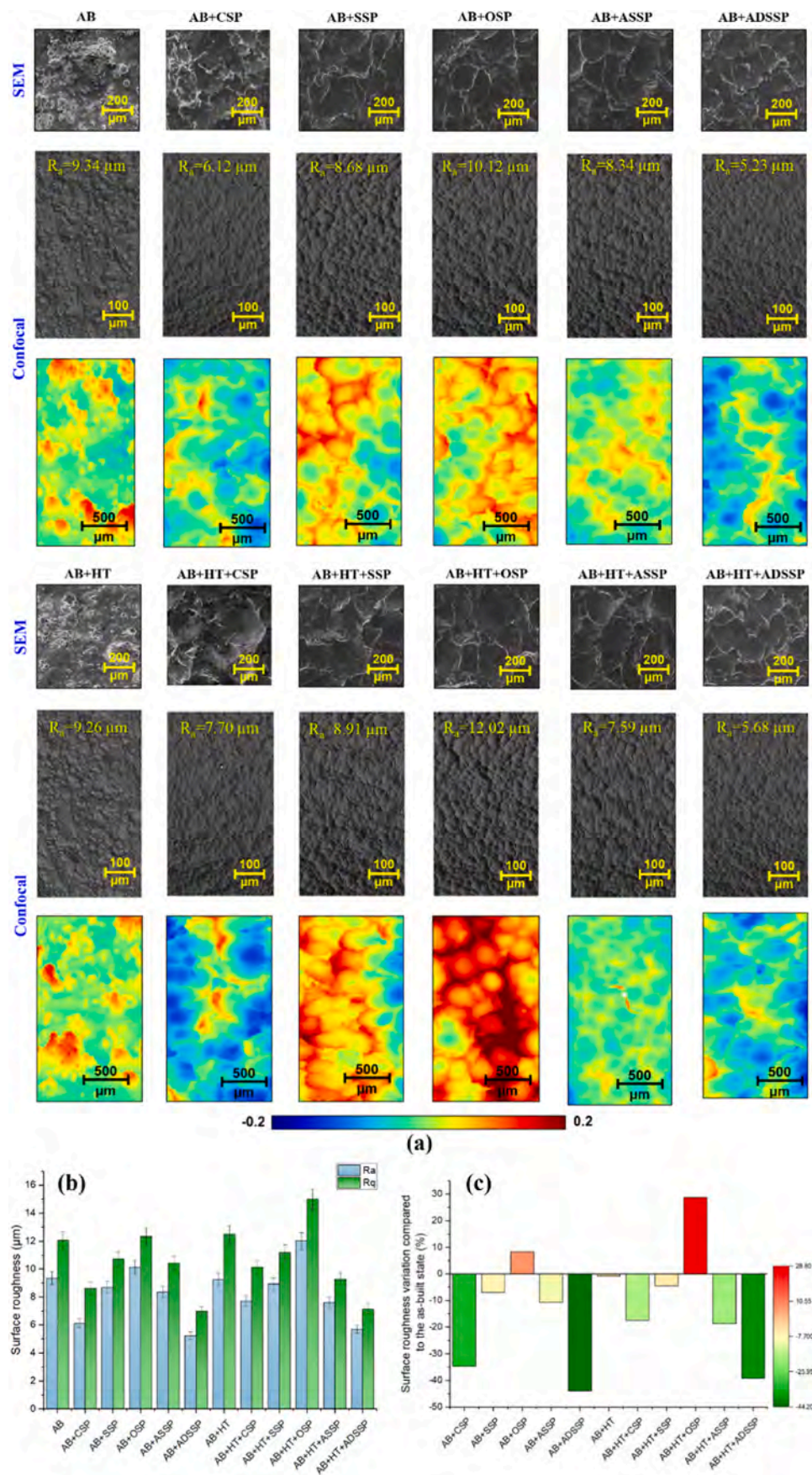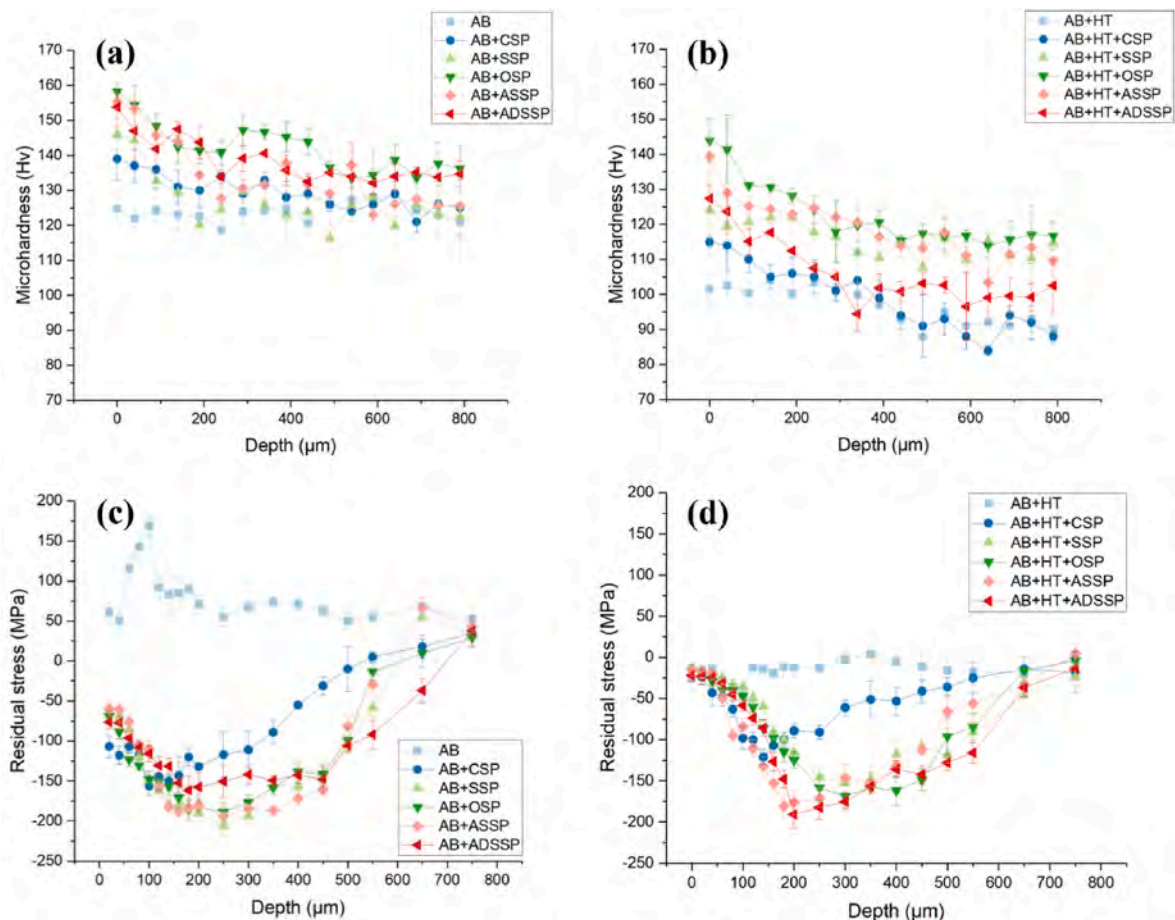
Fig. 8. (a) Surface morphologies of the as-built series and SP treated samples obtained from SEM and confocal morphological observations (b) Surface roughness in terms of R_a and R_q in all sets of samples (c) Comparison of the effects of each SP treatment on surface roughness variation in terms of R_a compared to the as-built state.

Fig. 9. Microhardness profiles for all sets of samples with initial (a) as-built and (b) heat-treated configurations; The distributions of residual stresses for all sets of samples with initial (a) as-built and (b) heat-treated states.

morphologies (similar to the ones in samples with treated SSP and OSP), a relatively smoother surface with hierarchical roughness is obtained. Dealing with ADSSP, a smoother surface with very low dimple-shaped surface morphology as well as lower hierarchical roughness was obtained. The first ascending stage is mainly used for applying plastic deformation. In contrast, besides inducing plastic deformation, the second descending stage primarily acts as a re-peening process to reduce surface roughness.

3.4. Microhardness and residual stress measurements

The microhardness profiles for the as-built and heat treated series are depicted in Fig. 9a and b, respectively. AB + HT samples, due to higher ductility and lower strength, demonstrated lower microhardness compared to the as-built series. In addition, shot peened samples exhibited significant surface layer hardening with the highest microhardness improvement on the top surface, gradually decreasing through the interior. This considerable surface layer grain refinement can be justified by forming gradient microstructural features and reducing grain size following the Hall-Petch relation [63]. Surface microhardness improvements of 11, 17, 26, 24, 23, 13, 22, 41, 37 and 25% were achieved for AB + CSP, AB + SSP, AB + ASSP, AB + ADSSP, AB + HT + CSP, AB + HT + SSP, AB + HT + ASSP and AB + HT + ADSSP samples, respectively. The results reveal higher hardness improvement in HT samples due to their lower strength.

Residual stress distributions from the top surface through the bulk material in the samples with as-built and heat-treated initial states are presented in Fig. 9c and d, respectively. It can be observed that the tensile residual stresses in the AB sample are released and transformed

into compressive ones in the AB + HT sample. In addition, shot peened samples exhibit high CRS with surface residual stresses of 55, -54, -43, -46, -45, -66, -25, -21, -12, -16, -15, -22 MPa measured for AB, AB + CSP, AB + SSP, AB + ASSP, AB + ADSSP, AB + HT, AB + HT + CSP, AB + HT + SSP, AB + HT + ASSP and AB + HT + ADSSP samples, respectively. Also, the highest maximum in-depth CRS of -156, -206, -189, -194, -162, -121, -152, -168, -180 and -190 MPa are determined for shot peened samples of AB + CSP, AB + SSP, AB + ASSP, AB + ADSSP, AB + HT + CSP, AB + HT + SSP, AB + HT + ASSP and AB + HT + ADSSP samples, respectively at a depth of 200–300 μm beneath the surface. Due to the gradual increase in the intensity of GSSP treatments induced, higher CRS, especially in the samples with a heat-treated initial state, were induced.

3.5. Fatigue behavior

As illustrated in Fig. 10a, rotating bending fatigue test results demonstrate that all the applied treatments, including SP processes and their combination with HT, positively influence the fatigue behavior of hourglass PBF-LB AlSi10Mg samples.

Due to its efficiency in microstructural homogenization, ductility improvement, and release of tensile residual stresses, the heat treatment enhanced the fatigue life. While SP improved the fatigue behavior due to sub-surface pores closure, surface roughness reduction, enhanced surface layer hardness, and inducing significant in-depth CRS. It should be mentioned that the hybrid HT + SP treatments exploit the positive effects of both surface and bulk treatments. Considering the fixed stress amplitude of 110 MPa, average fatigue lives of 1.95×10^5, 4.66×10^6, 5.71×10^6, 4.19×10^6, 6.98×10^6, 7.5×10^6, 5.51×10^4, 5.24×10^6,
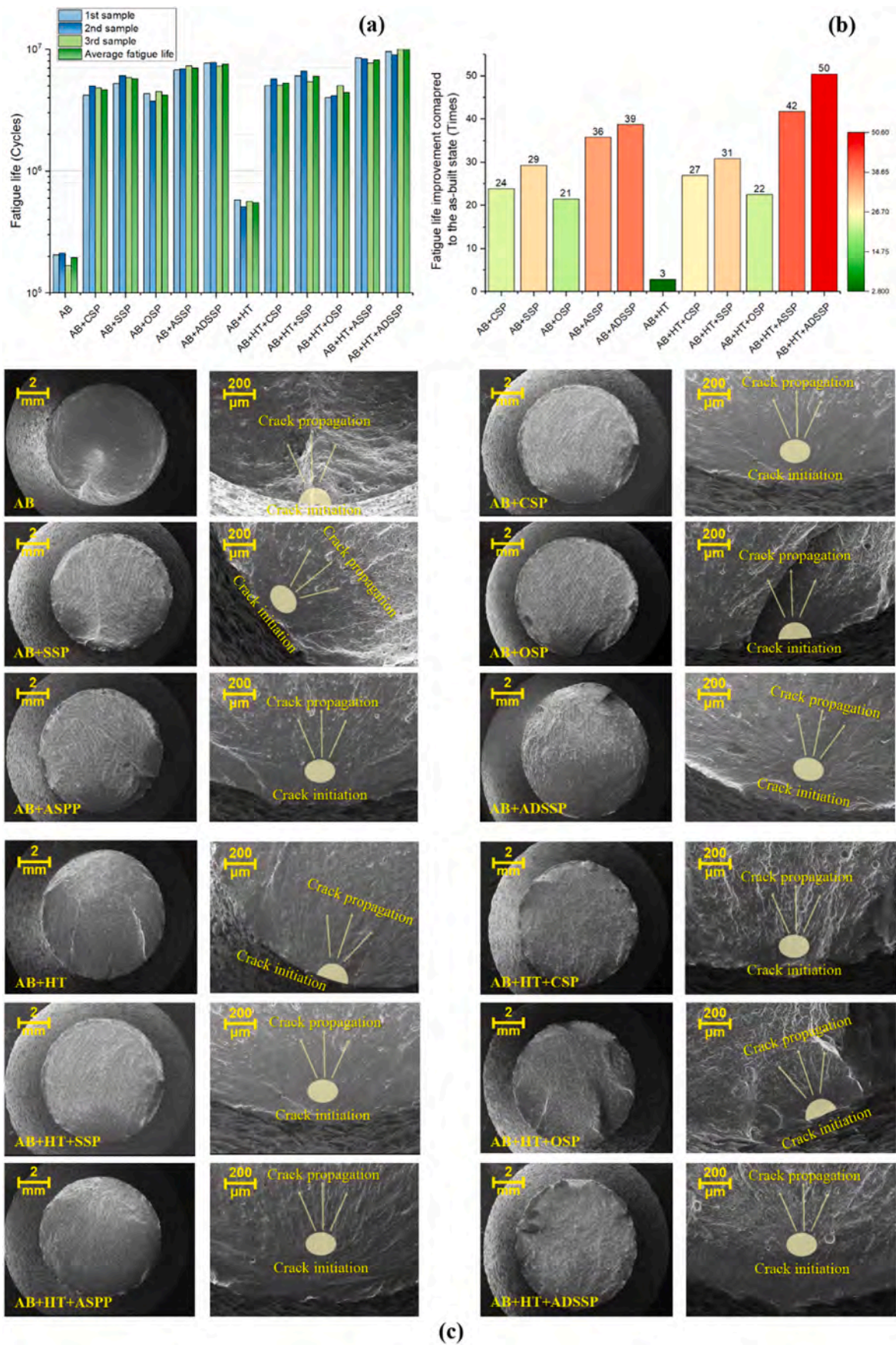
Fig. 10. (a) Rotating bending fatigue test results at a fixed stress amplitude of 110 MPa for all sets of samples (b) Fatigue life enhancement of post-processed samples compared with the as-built state. (c) SEM images of fracture surfaces of all sets of samples showing crack initiation site and crack propagation direction.

$4.38 \times 10^6, 8.15 \times 10^6$ and 9.84×10^6 cycles were obtained for AB, AB + CSP, AB + SSP, AB + ASSP, AB + ADSSP, AB + HT, AB + HT + CSP, AB + HT + SSP, AB + HT + ASSP and AB + HT + ADSSP samples, respectively. Although the OSP treatment increased the fatigue life compared to AB and AB + HT samples, it had the lowest efficiency compared with other SP processes (including CSP, SSP and GSSPs) due to the excessive surface roughness and formation of micro-crack surface defects.

Fig. 10b depicts the corresponding fatigue life improvement of post-processed samples compared with as-built and heat-treated states demonstrating that ADSSP had the highest efficiency in fatigue behavior enhancement followed by ASSP, SSP, CSP, and OSP, respectively.

The use of GSSP treatments resulted in further enhancements in fatigue behavior. This can be attributed to several factors. Firstly, the GSSP process led to a significant refinement of the surface layer grains, resulting in improved material strength and resistance to fatigue failure. Additionally, the GSSP treatments contributed to higher Si density in the surface layer. Moreover, GSSP treatments induced high levels of CRS at the surface and in-depth, which are known to increase the fatigue strength of the materials. The considerable depth achieved with closed sub-surface pores in GSSP treated samples also played a role in improving fatigue behavior by reducing the number of stress concentration sites and thus lowering the likelihood of crack initiation. Furthermore, GSSP treated samples exhibited lower surface roughness, which is beneficial for fatigue resistance as it reduces the risk of surface stress concentration and the initiation of fatigue cracks. In terms of specific performance improvements, the ADSSP treatment significantly enhanced fatigue life up to 38 times (AB + ADSSP) compared to the AB sample and 50 times (AB + HT + ADSSP) compared to the AB + HT sample. Similarly, the ASSP treatment improved fatigue life up to 35 times (AB + ASSP) compared to the AB sample and 41 times (AB + HT + ASSP) compared to the AB + HT sample. Although less than GSSP treatments, also the CSP and SSP treatments also showed substantial improvements, increasing fatigue life by approximately 25 and 30 times, respectively, compared to the AB and AB + HT conditions.

Fig. 10c represents the SEM images of the fracture surface of the failed samples after fatigue tests. In the AB, AB + OSP, AB + HT and AB + HT + OSP samples, the cracks initiated from the surface and propagated to the other side due to the very poor surface quality and high surface roughness. However, in the shot peened samples (both AB and HT configurations), similar sub-surface crack initiation patterns were observed due to high CRS.

4. Conclusions

As PBF-LB materials exhibit high internal and surface anomalies in as-built condition, applying favorable post-processing methods to address these imperfections to achieve higher performance in terms of mechanical properties is essential. The present study investigated the effect of a novel SP treatment named GSSP on PBF-LB AlSi10Mg for the first time to address the issues associated with common SP treatments. Comprehensive experimental analyses were conducted to highlight higher beneficial effects of GSSP compared to the preveisluy known SP processes of CSP, SSP and OSP. According to the obtained results, the following points can be concluded.

- GSSP, like the other high-energy SP treatments, can simultaneously form microstructural and chemical gradients in the top surface layer of the treated material. The formation of nanostructured grains in the surface layer with higher Si content led to increased surface layer hardening. The surface hardness after ASSP and ADSSP improved up to about 25% starting from the as-built condition and up to 37 and 25% starting from heat treated state, respectively.
- All the applied SP treatments positively affected sub-surface pore closure but to different extents. ASSP was the most efficient in pore closure with an affected depth of about 160 μm in both as-built and

heat treated states compared to the ADSSP with 102 and 121 μm depth in as-built and heat treated conditions, respectively. It should be noted that CSP could close the sub-surface porosities just up to the depth of 30 μm.
- The tensile surface residual stresses in the as-built configuration (55 MPa) were transformed to high CRS in the shot peened and heat treated series. All the considered SP treatments on samples with the as-built initial state (-43 to -66 MPa) and heat treated initial conditions (-12 to -25 MPa) were induced in the same range of CRS. ASSP and ADSSP treatments exhibited higher in-depth CRS up to -200 MPa in both as-built and heat treated conditions.
- ADSSP had the highest effect on surface roughness reduction, down to about 40% compared to initial as-built and heat treated states, followed by CSP/ASSP and SSP, respectively. At the same time, OSP increased the surface roughness due to the formation of high overlapping peaks and deep valleys on the surface. In the samples subjected to GSSP treatments, due to gradual variation of the projection pressure, which acted as a pre-hardening/smoothening stage for the subsequent pressures, a more uniform surface with shallower dimple-shaped surface morphologies can be obtained.
- ADSSP treatment exhibited the highest effectiveness for improved fatigue life, followed by ASSP, SSP, CSP, and OSP, respectively. GSSP treatments led to higher fatigue behavior enhancement due to the significant surface layer grain refinement, hardening and higher Si content, high surface and in-depth CRS, considerable depth with closed sub-surface pores, and lower surface roughness. ADSSP improved the fatigue life up to 38 and 50 times higher compared to the AB and AB + HT samples, respectively, and ASSP enhanced the fatigue life up to 35 and 41 times in comparison with AB and AB + HT series. While CSP and SSP improved the fatigue life up to about 25 and 30 times higher, respectively, compared to the AB and AB + HT states.

CRediT authorship contribution statement

Erfan Maleki: Conceptualization, Investigation, Formal analysis, Visualization, Writing – original draft. **Sara Bagherifard:** Conceptualization, Methodology, Validation, Writing – review & editing, Supervision. **Asghar Heydari Astaraee:** Formal analysis, Writing – review & editing. **Simone Sgarbazzini:** Investigation, Formal analysis. **Michele Bandini:** Investigation, Resources. **Mario Guagliano:** Conceptualization, Resources, Writing – review & editing, Supervision.

Declaration of competing interest

The authors declare that they have no known competing financial interests or personal relationships that could have appeared to influence the work reported in this paper.

Data availability

Data will be made available on request.

References

[1] D. Herzog, V. Seyda, E. Wycisk, C. Emmelmann, Additive manufacturing of metals, Acta Mater. 117 (2016) 371–392, https://doi.org/10.1016/j.actamat.2016.07.019.

[2] T. Mukherjee, W. Zhang, T. DebRoy, An improved prediction of residual stresses and distortion in additive manufacturing, Comput. Mater. Sci. 126 (2017) 360–372, https://doi.org/10.1016/j.commatsci.2016.10.003.

[3] A. Poudel, M.S. Yasin, J. Ye, J. Liu, Feature-based Volumetric Defect Classi Fi Ca-Tion in Metal Additive Manufacturing, 2022, pp. 1–12, https://doi.org/10.1038/s41467-022-34122-x.

[4] M.H. Nasab, D. Gastaldi, N.F. Lecis, M. Vedani, On morphological surface features of the parts printed by selective laser melting (SLM), Addit. Manuf. 24 (2018) 373–377, https://doi.org/10.1016/j.addma.2018.10.011.

[5] A.R. Balachandramurthi, J. Moverare, N. Dixit, R. Pederson, Influence of defects and as-built surface roughness on fatigue properties of additively manufactured

Alloy 718, Mater. Sci. Eng. 735 (2018) 463–474, https://doi.org/10.1016/j.msea.2018.08.072.

[6] E. Maleki, S. Bagherifard, M. Bandini, M. Guagliano, Surface post-treatments for metal additive manufacturing: progress, challenges, and opportunities, Addit. Manuf. 37 (2021), 101619, https://doi.org/10.1016/j.addma.2020.101619.

[7] E. Salvati, A.J.G. Lunt, S. Ying, T. Sui, H.J. Zhang, C. Heason, G. Baxter, A. M. Korsunsky, Eigenstrain reconstruction of residual strains in an additively manufactured and shot peened nickel superalloy compressor blade, Comput. Methods Appl. Mech. Eng. 320 (2017) 335–351, https://doi.org/10.1016/j.cma.2017.03.005.

[8] D.A. Lesyk, V.V. Dzhemelinskyi, S. Martinez, B.N. Mordyuk, A. Lamikiz, Surface shot peening post-processing of inconel 718 alloy parts printed by laser powder bed fusion additive manufacturing, J. Mater. Eng. Perform. 30 (2021) 6982–6995, https://doi.org/10.1007/s11665-021-06103-6.

[9] N. Alharbi, Corrosion resistance of 3D printed SS316L post-processed by ultrasonic shot peening at optimum energy level. https://doi.org/10.1177/09544054221112164, 2022.

[10] H. Soyama, Y. Okura, The use of various peening methods to improve the fatigue strength of titanium alloy Ti6Al4V manufactured by electron beam melting, AIMS Mater. Sci. 5 (2018) 1000–1015, https://doi.org/10.3934/MATERSCI.2018.5.1000.

[11] M. Sato, O. Takakuwa, M. Nakai, M. Niinomi, F. Takeo, H. Soyama, Using cavitation peening to improve the fatigue life of titanium alloy Ti-6Al-4V manufactured by electron beam melting, Mater. Sci. Appl. 7 (2016) 181–191, https://doi.org/10.4236/msa.2016.74018.

[12] X. Xing, X. Duan, T. Jiang, J. Wang, F. Jiang, Ultrasonic peening treatment used to improve stress corrosion resistance of AlSi10Mg components fabricated using selective laser melting, Metals 9 (2019), https://doi.org/10.3390/met9010103.

[13] A. Du Plessis, D. Glaser, H. Moller, N. Mathe, L. Tshabalala, B. Mfusi, R. Mostert, Pore closure effect of laser shock peening of additively manufactured AlSi10Mg, 3D print, Addit. Manuf. 6 (2019) 245–252, https://doi.org/10.1089/3dp.2019.0064.

[14] A.N. Jinoop, S.K. Subbu, C.P. Paul, I.A. Palani, Post-processing of laser additive manufactured inconel 718 using laser shock peening, Int. J. Precis. Eng. Manuf. 20 (2019) 1621–1628, https://doi.org/10.1007/s12541-019-00147-4.

[15] I. Yeo, S. Bae, A. Amanov, S. Jeong, Effect of laser shock peening on properties of heat-treated Ti–6Al–4V manufactured by laser powder bed fusion, Int. J. Precis. Eng. Manuf. - Green Technol. 8 (2021) 1137–1150, https://doi.org/10.1007/s40684-020-00234-2.

[16] Q. Jiang, S. Li, C. Zhou, B. Zhang, Y. Zhang, Effects of laser shock peening on the ultra-high cycle fatigue performance of additively manufactured Ti6Al4V alloy, Opt Laser. Technol. 144 (2021), https://doi.org/10.1016/j.optlastec.2021.107391.

[17] D.A. Lesyk, S. Martinez, B.N. Mordyuk, O.O. Pedash, V.V. Dzhemelinskyi, A. Lamikiz, Ultrasonic surface post-processing of hot isostatic pressed and heat treated superalloy parts manufactured by laser powder bed fusion, Addit. Manuf. Lett. 3 (2022), 100063, https://doi.org/10.1016/j.addlet.2022.100063.

[18] H. Zhang, J. Zhao, J. Liu, H. Qin, Z. Ren, G.L. Doll, Y. Dong, C. Ye, The effects of electrically-assisted ultrasonic nanocrystal surface modification on 3D-printed Ti-6Al-4V alloy, Addit. Manuf. (2018), https://doi.org/10.1016/j.addma.2018.04.035.

[19] E. Maleki, S. Bagherifard, O. Unal, S. Shao, N. Shamsaei, Assessing the efficacy of several impact-based mechanical techniques on fatigue behavior of additive manufactured AlSi10Mg, Mater. Sci. Eng. 872 (2023), 144940, https://doi.org/10.1016/j.msea.2023.144940.

[20] E. Maleki, S. Bagherifard, O. Unal, M. Bandini, M. Guagliano, The effects of microstructural and chemical surface gradients on fatigue performance of laser powder bed fusion AlSi10Mg, Mater. Sci. Eng. 840 (2022), 142962, https://doi.org/10.1016/j.msea.2022.142962.

[21] E. Maleki, S. Bagherifard, O. Unal, A. Jam, S. Shao, M. Guagliano, N. Shamsaei, Superior effects of hybrid laser shock peening and ultrasonic nanocrystalline surface modification on fatigue behavior of additive manufactured AlSi10Mg, Surf. Coating. Technol. 463 (2023), 129512, https://doi.org/10.1016/j.surfcoat.2023.129512.

[22] E. Maleki, S. Bagherifard, O. Unal, M. Bandini, M. Guagliano, On the effects of laser shock peening on fatigue behavior of V-notched AlSi10Mg manufactured by laser powder bed fusion, Int. J. Fatig. 163 (2022), 107035, https://doi.org/10.1016/j.ijfatigue.2022.107035.

[23] E. Maleki, S. Bagherifard, M. Guagliano, Correlation of residual stress, hardness and surface roughness with crack initiation and fatigue strength of surface treated additive manufactured AlSi10Mg: experimental and machine learning approaches, J. Mater. Res. Technol. 24 (2023) 3265–3283, https://doi.org/10.1016/j.jmrt.2023.03.193.

[24] E. Maleki, S. Bagherifard, F. Sabouri, M. Bandini, M. Guagliano, Hybrid thermal, mechanical and chemical surface post-treatments for improved fatigue behavior of laser powder bed fusion AlSi10Mg notched samples, Surf. Coating. Technol. 430 (2022), https://doi.org/10.1016/j.surfcoat.2021.127962.

[25] E. Maleki, S. Bagherifard, O. Unal, F. Sabouri, M. Bandini, M. Guagliano, Effects of different mechanical and chemical surface post-treatments on mechanical and surface properties of as-built laser powder bed fusion AlSi10Mg, Surf. Coating. Technol. 439 (2022), 128391, https://doi.org/10.1016/j.surfcoat.2022.128391.

[26] E. Maleki, O. Unal, M. Bandini, M. Guagliano, S. Bagherifard, Individual and synergistic effects of thermal and mechanical surface post-treatments on wear and corrosion behavior of laser powder bed fusion AlSi10Mg, J. Mater. Process. Technol. 302 (2022), 117479, https://doi.org/10.1016/j.jmatprotec.2021.117479.

[27] A.H. Maamoun, M.A. Elbestawi, S.C. Veldhuis, Influence of shot peening on alsi10mg parts fabricated by additive manufacturing, J. Manuf. Mater. Process. 2 (2018), https://doi.org/10.3390/jmmp2030040.

[28] E. Maleki, O. Unal, K. Reza Kashyzadeh, Efficiency analysis of shot peening parameters on variations of hardness, grain size and residual stress via taguchi approach, Met. Mater. Int. 25 (2019), https://doi.org/10.1007/s12540-019-00290-7.

[29] J. Wu, H. Liu, P. Wei, Q. Lin, S. Zhou, Effect of shot peening coverage on residual stress and surface roughness of 18CrNiMo7-6 steel, Int. J. Mech. Sci. 183 (2020), https://doi.org/10.1016/j.ijmecsci.2020.105785.

[30] Y. Todaka, M. Umemoto, Y. Watanabe, K. Tsuchiya, Formation of nanocrystalline structure in steels by air blast shot peening and particle impact processing, Mater. Sci. Forum 449–452 (2004) 1149–1152. https://doi.org/10.4028/www.scientific.net/msf.449-452.1149.

[31] S. Bagherifard, M. Guagliano, Fatigue behavior of a low-alloy steel with nanostructured surface obtained by severe shot peening, Eng. Fract. Mech. 81 (2012) 56–68, https://doi.org/10.1016/j.engfracmech.2011.06.011.

[32] E. Maleki, O. Unal, K. Reza Kashyzadeh, Surface layer nanocrystallization of carbon steels subjected to severe shot peening: analysis and optimization, Mater. Char. 157 (2019), https://doi.org/10.1016/j.matchar.2019.109877.

[33] E. Maleki, G.H. Farrahi, K. Reza Kashyzadeh, O. Unal, M. Gugaliano, S. Bagherifard, Effects of conventional and severe shot peening on residual stress and fatigue strength of steel AISI 1060 and residual stress relaxation due to fatigue loading: experimental and numerical simulation, Met. Mater. Int. 27 (2021) 2575–2591, https://doi.org/10.1007/s12540-020-00890-8.

[34] Y.G. Liu, M.Q. Li, Structure response characteristics and surface nanocrystallization mechanism of alpha phase in Ti-6Al-4V subjected to high energy shot peening, J. Alloys Compd. 773 (2019) 860–871, https://doi.org/10.1016/j.jallcom.2018.09.343.

[35] C. Zhang, M. Zheng, Y. Wang, P. Gao, B. Gan, Effect of high energy shot peening on the wear resistance of TiN films on a TA2 surface, Surf. Coating. Technol. 378 (2019), https://doi.org/10.1016/j.surfcoat.2019.07.045.

[36] C. Yang, Y.G. Liu, M.Q. Li, Characteristics and formation mechanisms of defects in surface layer of TC17 subjected to high energy shot peening, Appl. Surf. Sci. 509 (2020), https://doi.org/10.1016/j.apsusc.2019.144711.

[37] S. Pour-Ali, A.R. Kiani-Rashid, A. Babakhani, S. Virtanen, M. Allieta, Correlation between the surface coverage of severe shot peening and surface microstructural evolutions in AISI 321: a TEM, FE-SEM and GI-XRD study, Surf. Coating. Technol. 334 (2018) 461–470, https://doi.org/10.1016/j.surfcoat.2017.11.062.

[38] E. Maleki, N. Maleki, A. Fattahi, O. Unal, M. Guagliano, S. Bagherifard, Mechanical characterization and interfacial enzymatic activity of AISI 316L stainless steel after surface nanocrystallization, Surf. Coating. Technol. 405 (2021), https://doi.org/10.1016/j.surfcoat.2020.126729.

[39] Y.K. Gao, Influence of shot peening on tension-tension fatigue property of two high strength Ti alloys, Surf. Eng. 22 (2006) 299–303, https://doi.org/10.1179/174329406X122865.

[40] G.D. Byrne, L. O'Neill, B. Twomey, D.P. Dowling, Comparison between shot peening and abrasive blasting processes as deposition methods for hydroxyapatite coatings onto a titanium alloy, Surf. Coating. Technol. 216 (2013) 224–231, https://doi.org/10.1016/j.surfcoat.2012.11.048.

[41] L. Trško, M. Guagliano, O. Bokůvka, F. Nový, Fatigue Life of AW 7075 Aluminium Alloy after Severe Shot Peening Treatment with Different Intensities, Procedia Eng., 2014, pp. 246–252, https://doi.org/10.1016/j.proeng.2014.06.257.

[42] E. Maleki, O. Unal, K.R. Kashyzadeh, Effects of conventional, severe, over, and re-shot peening processes on the fatigue behavior of mild carbon steel, Surf. Coating. Technol. 344 (2018) 62–74, https://doi.org/10.1016/j.surfcoat.2018.02.081.

[43] Y. Wang, H. Xie, Z. Zhou, X. Li, W. Wu, J. Gong, Effect of shot peening coverage on hydrogen embrittlement of a ferrite-pearlite steel, Int. J. Hydrogen Energy 45 (2020) 7169–7184, https://doi.org/10.1016/j.ijhydene.2020.01.021.

[44] E. Maleki, S. Bagherifard, O. Unal, M. Bandini, G.H. Farrahi, M. Guagliano, Introducing gradient severe shot peening as a novel mechanical surface treatment, Sci. Rep. 11 (2021), 22035, https://doi.org/10.1038/s41598-021-01152-2.

[45] S. Bagherifard, N. Beretta, S. Monti, M. Riccio, M. Bandini, M. Guagliano, On the fatigue strength enhancement of additive manufactured AlSi10Mg parts by mechanical and thermal post-processing, Mater. Des. 145 (2018) 28–41, https://doi.org/10.1016/j.matdes.2018.02.055.

[46] E. Maleki, S. Bagherifard, S.M.J. Razavi, M. Riccio, M. Bandini, A. du Plessis, F. Berto, M. Guagliano, Fatigue behaviour of notched laser powder bed fusion AlSi10Mg after thermal and mechanical surface post-processing, Mater. Sci. Eng. 829 (2022), 142145, https://doi.org/10.1016/j.msea.2021.142145.

[47] Sae International, Procedures for using standard shot peening test strip, SAE Stand J443 (2003).

[48] E. Maleki, S. Bagherifard, L. Rovatti, R. Michael, M. Revuru, M. Guagliano, Developing a best practice for sample preparation of additive manufactured AlSi10Mg for electron backscatter diffraction analysis, Addit. Manuf. Lett. 5 (2023), 100122, https://doi.org/10.1016/j.addlet.2023.100122.

[49] F.H. Kim, S.P. Moylan, E.J. Garboczi, J.A. Slotwinski, Investigation of pore structure in cobalt chrome additively manufactured parts using X-ray computed tomography and three-dimensional image analysis, Addit. Manuf. 17 (2017) 23–38, https://doi.org/10.1016/j.addma.2017.06.011.

[50] International Organization for Standardization, ISO 25178-2: Geometrical Product Specifications (GPS) - Surface Texture: Areal Part - 2: Terms, Definitions and Surface Texture Parameters, 2007.

[51] L. Thijs, K. Kempen, J.P. Kruth, J. Van Humbeeck, Fine-structured aluminium products with controllable texture by selective laser melting of pre-alloyed AlSi10Mg powder, Acta Mater. 61 (2013) 1809–1819, https://doi.org/10.1016/j.actamat.2012.11.052.

[52] A. Hadadzadeh, B.S. Amirkhiz, J. Li, M. Mohammadi, Columnar to equiaxed transition during direct metal laser sintering of AlSi10Mg alloy: effect of building

direction, Addit. Manuf. 23 (2018) 121–131, https://doi.org/10.1016/j.addma.2018.08.001.

[53] A. Basak, S. Das, Epitaxy and microstructure evolution in metal additive manufacturing, Annu. Rev. Mater. Res. 46 (2016) 125–149, https://doi.org/10.1146/annurev-matsci-070115-031728.

[54] F. Alghamdi, X. Song, A. Hadadzadeh, B. Shalchi-Amirkhiz, M. Mohammadi, M. Haghshenas, Post heat treatment of additive manufactured AlSi10Mg: on silicon morphology, texture and small-scale properties, Mater. Sci. Eng. 783 (2020), https://doi.org/10.1016/j.msea.2020.139296.

[55] X. Liang, Z. Liu, Q. Wang, B. Wang, X. Ren, Tool wear-induced microstructure evolution in localized deformation layer of machined Ti–6Al–4V, J. Mater. Sci. 55 (2020) 3636–3651, https://doi.org/10.1007/s10853-019-04214-z.

[56] A.E. Davis, J.R. Hönnige, F. Martina, P.B. Prangnell, Quantification of strain fields and grain refinement in Ti-6Al-4V inter-pass rolled wire-arc AM by EBSD misorientation analysis, Mater. Char. 170 (2020) 151–155, https://doi.org/10.1016/j.matchar.2020.110673.

[57] C. peng Liu, R. ming Ren, D. yi Liu, X. juan Zhao, C. huan Chen, An EBSD investigation on the evolution of the surface microstructure of D2 wheel steel

during rolling contact fatigue, Tribol. Lett. 68 (2020), https://doi.org/10.1007/s11249-020-1277-1.

[58] H. Torabian, J.P. Pathak, S.N. Tiwari, Wear characteristics of Al-Si alloys, Wear 172 (1994) 49–58, https://doi.org/10.1016/0043-1648(94)90298-4.

[59] C. Butler, S. Babu, R. Lundy, R. O'Reilly Meehan, J. Punch, N. Jeffers, Effects of processing parameters and heat treatment on thermal conductivity of additively manufactured AlSi10Mg by selective laser melting, Mater. Char. 173 (2021), https://doi.org/10.1016/j.matchar.2021.110945.

[60] D.K. Dwivedi, Wear behaviour of cast hypereutectic aluminium silicon alloys, Mater. Des. 27 (2006) 610–616, https://doi.org/10.1016/j.matdes.2004.11.029.

[61] D. Knoop, A. Lutz, B. Mais, A. von Hehl, A tailored AlSiMg alloy for laser powder bed fusion, Metals 10 (2020), https://doi.org/10.3390/met10040514.

[62] T. Kimura, T. Nakamoto, M. Mizuno, H. Araki, Effect of silicon content on densification, mechanical and thermal properties of Al-xSi binary alloys fabricated using selective laser melting, Mater. Sci. Eng. 682 (2017) 593–602, https://doi.org/10.1016/j.msea.2016.11.059.

[63] E.O. Hall, The deformation and ageing of mild steel: III Discussion of results, Proc. Phys. Soc. B 64 (1951) 747–753, https://doi.org/10.1088/0370-1301/64/9/303.